Available online at www.sciencedirect.com
ScienceDirect
Journal of the European Ceramic Society 28 (2008) 1149–1160
www.elsevier.com/locate/jeurceramsoc

Interfacial reaction behavior and thermal stability of barium zirconate-coated alumina fiber/alumina matrix composites

Zhong-Chun Chen [a,*], T. Tamachi [a], R. Kulkarni [b], K.K. Chawla [b], M. Koopman [b]

[a] *Department of Materials Science and Engineering, School of Engineering, Tohoku University, Aoba-yama 6-6-02, Aoba-ku, Sendai 980-8579, Japan*
[b] *Department of Materials Science and Engineering, University of Alabama at Birmingham, BEC 254, 1530 Third Avenue South, Birmingham, AL 35294, USA*

Received 20 May 2007; received in revised form 3 September 2007; accepted 8 September 2007
Available online 26 November 2007

Abstract

A barium zirconate ($BaZrO_3$) coating was incorporated onto surfaces of alumina fibers, and the coated alumina fiber/alumina matrix composites were prepared by hot pressing. The interfacial reactions between $BaZrO_3$ coating and Al_2O_3 fiber/matrix during the consolidation resulted in formation of ZrO_2 and Ba–β-Al_2O_3, one of nonstoichiometric hexaluminate compounds. The diffusion of Ba cations dominates the reaction process between $BaZrO_3$ coating and Al_2O_3 fiber/matrix. The Ba–β-Al_2O_3 phase exhibited an elongated morphology due to preferred orientational growth through directional diffusion and mass transport of Ba along the basal plane. The Young's modulus and hardness of the Ba–β-Al_2O_3 phase were measured by nanoindentation technique to be 250 GPa and 20 GPa, respectively. The $BaZrO_3$-coated Al_2O_3 fiber/Al_2O_3 matrix composites showed good microstructural stability during thermal exposure up to 1400 °C.

Keywords: Al_2O_3; Composites; Fibers; Interfaces; Nanoindentation; $BaZrO_3$

1. Introduction

Fiber reinforced ceramic matrix composites (CMCs) have attracted growing interest for high-temperature structural applications in gas turbine and aerospace engines, heat exchangers, hot gas filters, and thermal protection systems.[1–7] For example, in gas turbine engines, such components as blades, nozzles, and combustor liners, are conventionally made from nickel-based superalloys with operating temperatures around 1100 °C which is near their applicable upper temperature. Accordingly, the use of cooling air is necessary, thus leading to reduced efficiency and performance of the turbines. Since these applications require long-term exposure to oxidizing environments, the materials need to have a combination of mechanical (*e.g.*, strength, fracture toughness, and creep resistance), chemical (*e.g.*, oxidation and corrosion resistance), thermo-physical properties (*e.g.*, thermal shock resistance), and also long-term stability during service at elevated temperatures.[8] An all-oxide ceramic matrix composite consisting of oxide fibers, oxide matrix, and an oxide interphase(s), is a potential candidate due to its damage tolerance and inherent resistance to degradation in oxidizing atmospheres at high temperatures. Because of a reduced need or no need for cooling air, the applications of all-oxide CMCs lead to an increase in thermal efficiency and a reduction in pollutant emissions (NO_x, CO, and unburned hydrocarbons).

A tailored interphase, or interface between fibers and surrounding matrix, plays a crucial role in determining the mechanical properties such as strength and fracture toughness of a composite. An interphase must be weak enough to allow fiber/matrix interfacial debonding and subsequent fiber pullout during fracture.[9] A weak fiber/matrix interfacial layer in CMCs is generally obtained through incorporation of a coating on fibers. In oxide/oxide systems, various oxide compounds have been proposed as candidates for coating materials, which can be roughly divided into three classes. (1) Simple

* Corresponding author. Tel.: +81 22 795 7346; fax: +81 22 795 7346.
E-mail address: czc@material.tohoku.ac.jp (Z.-C. Chen).

0955-2219/$ – see front matter © 2007 Elsevier Ltd. All rights reserved.
doi:10.1016/j.jeurceramsoc.2007.09.048

oxides, such as SnO_2,[10–12] ZrO_2,[13,14] TiO_2,[15] and CeO_2.[16] (2) Complex oxides which have a high probability of low cohesion with matrix or fiber due to polarization of oxygen bonds by high valence cations.[17] These are exemplified by vanadates, phosphates or niobates, having a general formula MXO_4 (M = La, Y or Nd; X = P, Nb or V).[18–22] (3) Hexaluminates with a layered crystal structure, such as $CaAl_{12}O_{19}$ and $LaAl_{11}O_{18}$.[23–25] These oxide coatings are chemically inert at elevated temperatures with respect to both Al_2O_3 fiber and Al_2O_3 matrix.

Of particular interest for promising interphases is hexaluminates with hexagonal β-Al_2O_3 or magnetoplumbite (MP) structures because of their layered and cleavable structure similar to graphite and boron nitride, and a high anisotropy in fracture resistance.[26] Many alkali, alkaline-earth, and rare-earth cations can stabilize the hexaluminate structure in either β-Al_2O_3 or MP form.[27,28] Research work on $CaAl_{12}O_{19}$ and $LaAl_{11}O_{18}$ as candidates of coating materials has been reported.[23–25,29–33] For example, $CaAl_{12}O_{19}$ (hibonite) interphase can be aligned such that the basal cleavage planes are parallel to the fiber/matrix interface. The crack deflection and propagation via basal cleavage with the $CaAl_{12}O_{19}$ interphase has been observed.[29] Besides, Cain et al.[34] proposed an *in situ* reaction approach through reactions between a simple fiber coating and surrounding matrix to obtain a hexaluminate interphase. They applied a ceria-doped zirconia interface coating to Al_2O_3 fiber surface. During subsequent heat treatment, the reactions between the coating and Al_2O_3 result in formation of oriented hexaluminate $Ce_2O_3{\cdot}11Al_2O_3$ which can act as a low fracture energy interface barrier for crack deflection in Al_2O_3/Al_2O_3 composites.

Barium zirconate ($BaZrO_3$) has a cubic perovskite structure and a high melting point (~2600 °C). Gladysz et al.[35] investigated the processing and microstructural development of $Al_2O_3/BaZrO_3$ laminated composites. During hot pressing, $BaZrO_3$ reacts with Al_2O_3 to form a series of oxides: ZrO_2, $BaO{\cdot}Al_2O_3$, and $BaO{\cdot}6Al_2O_3$. Such reactions result in the formation of multiple, weak, and stable interfaces and hence cause crack deflection with corresponding potential improvements in fracture toughness. Further, the feasibility of $BaZrO_3$ as a candidate material for interfacial coating in Al_2O_3 fiber/Al_2O_3 matrix composites has been examined.[36] Unlike common interphase materials, where reactions between interphase and fiber/matrix are not desirable, a $BaZrO_3$ coating forms multiple interfaces through reactions with Al_2O_3 (both the fiber and matrix) during fabrication of the composites. As a result of these chemical reactions, ZrO_2 and Ba–β-Al_2O_3, one of hexaluminate compounds, are formed in the composites.[37,38]

In the present work, Ba–β-Al_2O_3 has been incorporated into Al_2O_3 fiber/Al_2O_3 matrix composites by $BaZrO_3$ coating on Al_2O_3 fibers and subsequent *in situ* interfacial reactions between the $BaZrO_3$ coating layer and Al_2O_3 fiber/matrix during processing of the composites. The objective was to further clarify the interfacial reaction behavior, morphology and mechanical properties of the reaction products in the composites, and their microstructural stability during thermal exposure at elevated temperatures.

2. Experimental procedure

2.1. Materials

The reinforcement used in this investigation was Nextel™ 610 Al_2O_3 fibers (3M Corp., St. Paul, MN), woven into eight-harness satin fabrics. The fibers are composed of fine-grained (<0.5 μm) polycrystalline α-Al_2O_3 (>99 wt%) with diameter between 10 μm and 12 μm, and the tows in a fabric contain approximately 400 filaments. Al_2O_3 powder with 99.99% purity and an average particle size of ~1 μm (Baikowski Inter. Corp., Charlotte, NC) was used to form the matrix of composites. As a source of $BaZrO_3$ coating, barium acetate and zirconium *n*-propanol were used.

2.2. Fiber coating, preparation of composites, and heat treatment

$BaZrO_3$ was used as a coating material in this work. The process to incorporate coating onto the surfaces of Al_2O_3 fibers involved the use of a sol, which was transformed to a required crystalline compound $BaZrO_3$ upon heating above the crystallization temperature. $BaZrO_3$ precursor was prepared from barium acetate and Zr–*n*-propanol by a sol–gel technique. The procedures used in synthesizing the $BaZrO_3$ precursor have been described elsewhere.[37] Small pieces of fabric, measuring 28 mm × 41 mm, were desized at 800 °C and then injected with $BaZrO_3$ aqueous sol by means of a syringe. The coated fabric pieces were dried with a heat gun to produce a dry gel containing Ba, Zr, and organic compounds, followed by calcining at 800 °C for 1 h in air. The coating operation was made twice (repeated a second time with the same procedure stated above) to obtain thick coating layers.

The $BaZrO_3$-coated fabrics and Al_2O_3 powder were arranged in a laminated structure within a graphite die and consolidated via uniaxial hot pressing. The fabric planes were perpendicular to the loading direction during hot pressing. The hot pressing was performed under vacuum at 1300 °C for 1 h at a pressure of 35 MPa. To examine the thermal stability of the composites at elevated temperatures, some hot-pressed specimens were isothermally heat-treated in air in a temperature range of 1000–1600 °C for 24 h.

2.3. Characterization

The phase identifications for hot-pressed composites were performed by X-ray diffraction (XRD) with Cu Kα radiation. Microstructural characterization was carried out by scanning electron microscopy (SEM) with an energy-dispersive X-ray spectroscopy (EDS). In addition, electron probe microanalyzer (EPMA) was used for compositional analysis.

The micromechanical properties of different phases in the composites, such as Young's modulus and hardness, were evaluated by a nanoindentation technique using Nanoindenter XP (MTS Systems). The indenter used was a three-sided pyramidal Berkovich diamond tip with a nominal radius of 50 nm. A constant penetration depth of 1200 nm was used in all indentation

experiments. Multiple measurements were made by selecting an array of regularly spaced indentations with a 10 μm spacing between indents. The elastic response of the machine (frame compliance) was calibrated using a silica standard. A continuous stiffness measurements (CSM) technique,[39] which allows the measurement of contact stiffness at any point along the loading curve, was used to obtain continuous measurements of elastic modulus and hardness of various phases in the composites with displacement of the indenter. The indentation positions were determined by an optical microscope prior to indentation measurements. After indentation, indenter craters were examined by SEM to ensure that indentation took place in a single phase.

To evaluate the effect of thermal exposure, a parameter of damage in Young's modulus (D_E) was calculated according to following formula [40]

$$D_E = 1 - \left(\frac{E}{E_0}\right) \quad (1)$$

where E_0 and E are Young's modulus values of the composites before and after heat treatment, respectively. The Young's modulus was determined via an impulse excitation technique (GrindoSonic MK5, J.W. Lemmens, St. Louis, MO). By measuring the resonant frequency of a rectangular bar tested in the flexural mode of vibration, the dynamic Young's modulus could be obtained.

3. Results

3.1. Interfacial reactions and microstructure of hot-pressed composites

Fig. 1(a) shows a typical SEM image in backscattered electron mode on a polished cross-section (perpendicular to the fabric plane) of a $BaZrO_3$-coated Al_2O_3 fiber/Al_2O_3 matrix composite hot-pressed at 1300 °C. White, light gray, and dark gray features can be observed in the micrograph. The dark gray regions correspond to Al_2O_3 fibers or Al_2O_3 matrix as identified by EDS analysis shown in Fig. 1(b), while the white ones, present at the interfaces between fibers, are associated with the initial coating layers. The incorporation of $BaZrO_3$ coating significantly impeded the sintering or joining between fiber and fiber as well as between fiber and matrix. XRD analysis showed that almost no $BaZrO_3$ phase remained and only three phases, Al_2O_3, monoclinic ZrO_2, and $BaO{\cdot}7.3Al_2O_3$ (*i.e.*, $BaAl_{14.66}O_{23}$ or the so-called Ba–β-Al_2O_3), were detected in the hot-pressed samples. This indicates that the reactions between $BaZrO_3$ coating and Al_2O_3 fiber/matrix occur during the processing (hot pressing) of the composites.

EDS analysis (Fig. 1(b)) showed that the white regions, such as the region 2 marked in Fig. 1(a), consisted mainly of Zr, Al, and O as well as extremely low Ba. This reveals that the white phase, distributed at the interfaces between fibers, is a Zr-rich

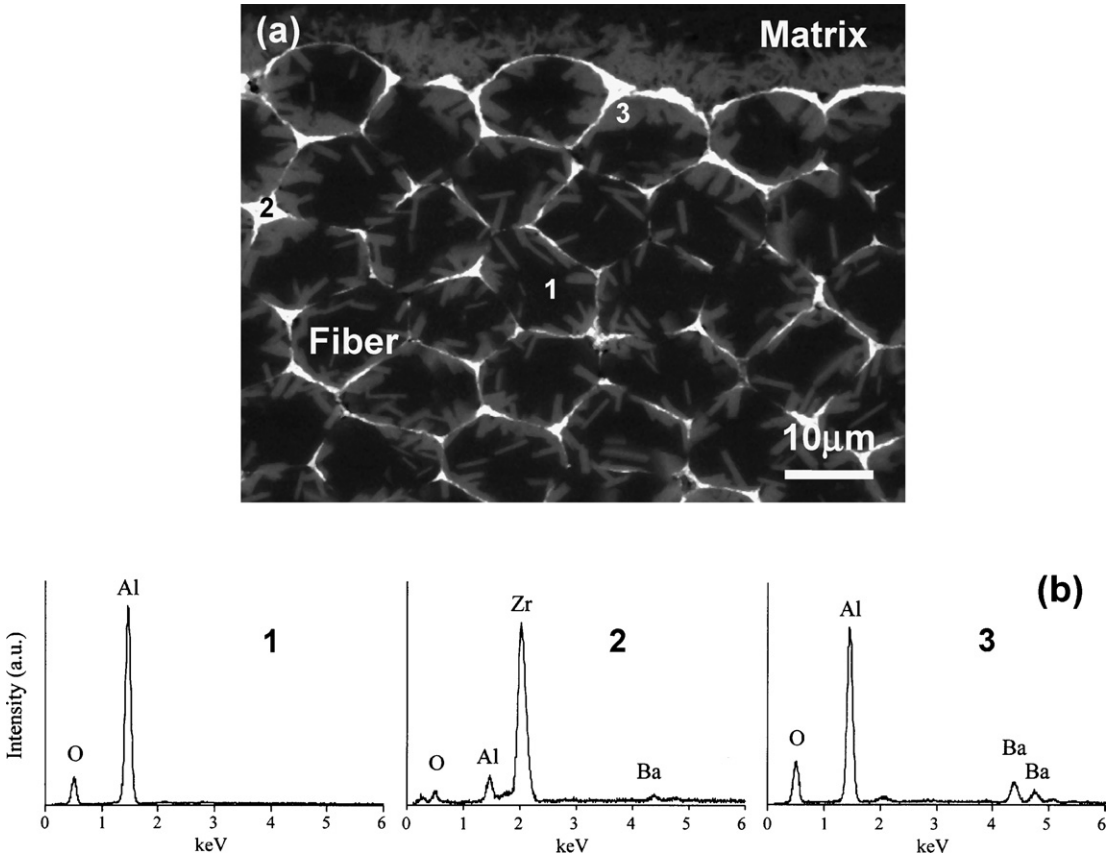

Fig. 1. (a) SEM image in backscattered electron mode showing the microstructure of $BaZrO_3$-coated Al_2O_3 fiber/Al_2O_3 matrix composite hot-pressed at 1300 °C and (b) EDS spectra corresponding to the positions marked with numbers in (a).

and Ba-poor phase. It was observed from Fig. 1(a) that there were a large number of elongated particles or platelets (light gray regions) around fiber/fiber and fiber/matrix interfaces. At triple points among three fibers, where more coating material was incorporated due to larger interfiber spaces, many platelets formed and combined together, resulting in occurrence of large reaction zones with light gray contrast near fiber surfaces or interfaces between fibers. In addition to Al and O, these platelets (*e.g.*, region 3 in Fig. 1(a)) contained more Ba (Ba-rich), indicating the diffusion of Ba from $BaZrO_3$ coating layers. From XRD and EDS results, it would appear that the Zr-rich and Ba-rich phases are related to ZrO_2 and Ba–β-Al_2O_3, respectively.

The elemental distributions in hot-pressed specimens were also examined by EPMA (Fig. 2). For the microstructure shown in Fig. 2(d), the corresponding elemental distribution maps of Zr, Ba, and Al are shown in Fig. 2(a)–(c), respectively. A comparison of the microstructure and Zr distribution map shows that Zr was mainly present at the interfaces between fibers, *i.e.*, distributed in the initial coating layers. This confirms again that the phase with a white contrast shown in Figs. 1(a) and 2(d) is a Zr-rich phase. Moreover, it was observed from Fig. 2(a) that the concentrations of Zr in the Zr-rich areas were not homogeneous. For those places with thicker coating layers (typically triple points among fibers), there were higher Zr concentrations in the central regions. For example, for an area marked with an arrow in Fig. 2(d), the "line" analysis (actually a narrow range between two lines shown in Fig. 2) showed that the concentration of Zr was ~53%, about 16 times higher than those places with lower Zr contents.

With regard to Ba (Fig. 2(b)), its distribution was quite different from that of Zr. There existed a lot of Ba inside Al_2O_3 fibers, and Ba was distributed in some directions preferentially, other than uniformly diffusing into fibers or matrix around the coating layers. The distribution of Ba was also inhomogeneous in the Ba-rich platelets. In particular, there was higher amount of Ba in those larger reaction areas.

From the above results, it can be concluded that the white regions in Fig. 1(a) correspond primarily to ZrO_2, while elongated particles with a light gray contrast arise from the Ba–β-Al_2O_3 compound. In comparison with Zr and Al, Ba exhibited much larger diffusion distance and preferred directional distribution.

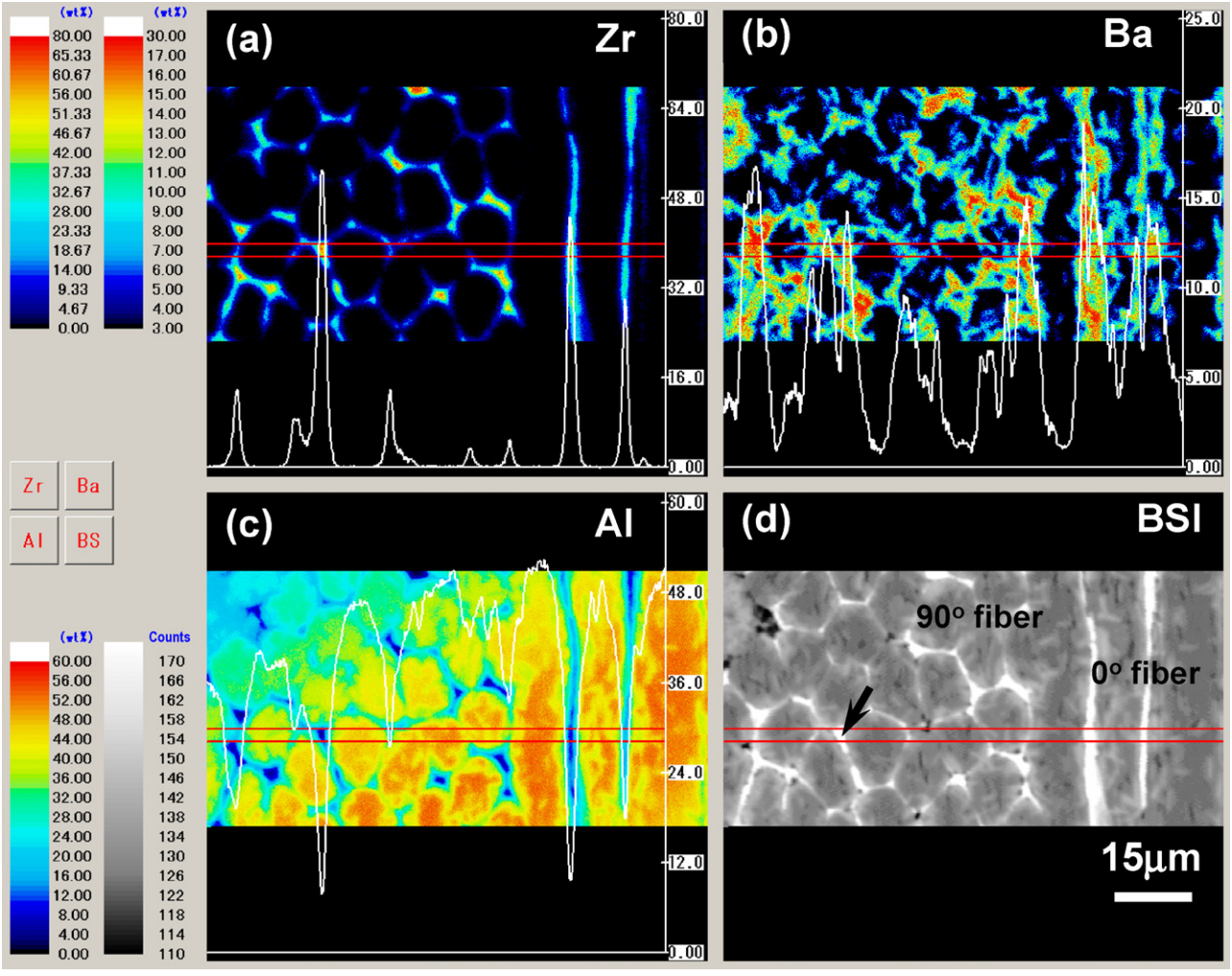

Fig. 2. Elemental distribution maps of (a) Zr, (b) Ba, and (c) Al as well as (d) corresponding backscattered electron image for a hot-pressed composite, analyzed by EPMA.

3.2. Micromechanical properties of interfacial reaction products

Because of a lack of mechanical property data on the Ba–β-Al_2O_3 phase in literature, nanoindentation measurements have been carried out to evaluate the micromechanical properties of the Ba–β-Al_2O_3 phase, formed by interfacial reactions between $BaZrO_3$ coating and Al_2O_3 fiber/matrix. Fig. 3 shows representative load versus displacement curves during loading and unloading for Al_2O_3 matrix and Ba–β-Al_2O_3 reinforcements. For the Ba–β-Al_2O_3 phase, the measurement was made in a reaction zone near the surface of a 90° fiber. The Ba–β-Al_2O_3 phase showed a larger penetration depth than Al_2O_3 at a given load, showing that Ba–β-Al_2O_3 has a lower hardness level. It appears that there are some small "pop-ins", displacement discontinuities in the load–displacement curves during loading, as indicated by arrows in Fig. 3. Furthermore, the Al_2O_3 matrix has more discontinuities, compared to the Ba–β-Al_2O_3 phase. These pop-ins may be attributed to the generation of microcracks and/or small-scale surface damages. The pop-in phenomenon has also been identified in sintered polycrystalline alumina [41,42] and alumina films produced by combustion CVD technique.[43]

The Young's modulus and hardness of the Ba–β-Al_2O_3 phase, obtained via nanoindentation measurements, are plotted in Fig. 4 as a function of displacement. Both the modulus and hardness had respective "plateau" regime at above ~200 nm up to ~1100 nm, independent of the depth into the sample. The hardness reached a larger value at ~100 nm and then dropped to a stable "plateau". Taking a depth range of 200–1100 nm (Fig. 4), one can obtain average values of Young's modulus and hardness, being 250 GPa and 20 GPa, respectively. The results of nanoindentation measurements for Al_2O_3 fiber, Al_2O_3 matrix, and Ba–β-Al_2O_3 phase are summarized in Table 1. The data for Al_2O_3 are in good agreement with those reported in the literature.[1]

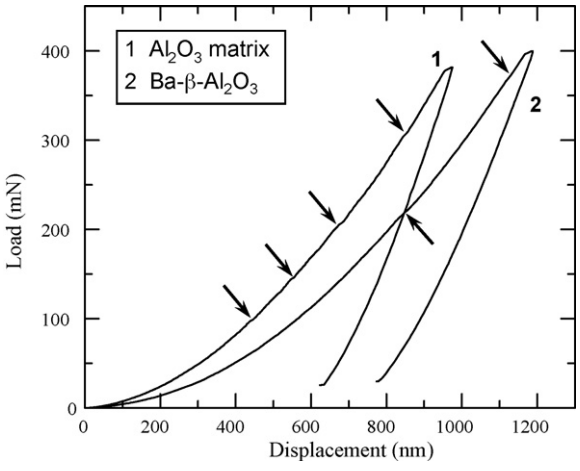

Fig. 3. Representative load versus displacement curves during loading and unloading for Al_2O_3 matrix and Ba–β-Al_2O_3. Note the presence of "pop-ins" (marked with arrows) on the loading curves.

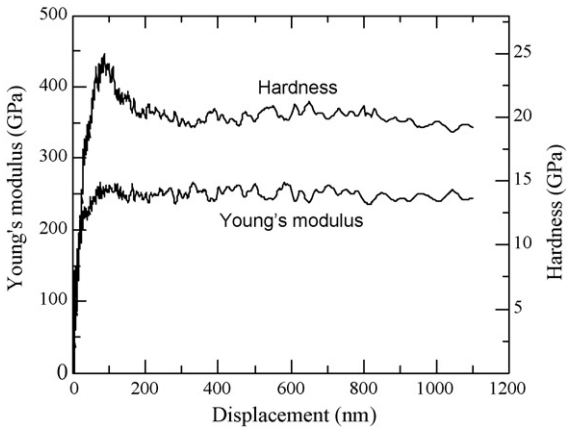

Fig. 4. Young's modulus and hardness of Ba–β-Al_2O_3 phase as a function of penetration depth, measured by a nanoindentation technique.

3.3. Effect of heat treatment on microstructural stability

To examine the microstructural stability of $BaZrO_3$-coated Al_2O_3 fiber/Al_2O_3 matrix composites, the hot-pressed specimens were exposed in air at elevated temperatures. Fig. 5 shows the microstructures of the specimens hot-pressed at 1300 °C, followed by heat treatment for 24 h at different temperatures ranging from 1200 °C to 1600 °C. Note that the microstructural observations were carried out after polishing a few micrometers of surface layers of the heat-treated specimens. At 1200 °C (Fig. 5(a)), the microstructure was similar to that of as-hot-pressed specimen (Fig. 1(a)), and no evident microstructural change could be identified. When the heat treatment was conducted at 1400 °C (Fig. 5(b)), a slight change was observed for ZrO_2 phase located at the interfaces between Al_2O_3 fibers. The surfaces of ZrO_2 phase started to be disturbed. For example, continuous ZrO_2 with rodlike shape tended to be broken up, and its continuity started to be decreased. It appeared that those ZrO_2 rods with smaller diameters were broken up easily. Concurrent with the morphological change of ZrO_2, some elongated Ba–β-Al_2O_3 particles became larger in width, and some particles were combined into large reaction zones.

At 1500 °C (Fig. 5(c)), such microstructural changes became more evident, and a large number of equiaxed ZrO_2 particles, generated through breakup of continuous rodlike ZrO_2 phase, were observed. In addition, some incompletely broken up or residual rodlike ZrO_2 particles were still present. These ZrO_2 particles were distributed at the interfaces between Al_2O_3 fibers. As shown in Fig. 5(c), more Ba–β-Al_2O_3 phase with light gray contrast has been formed, which gradually penetrated into the fibers. When the exposure temperature was raised to 1600 °C (Fig. 5(d)), the average size of ZrO_2 particles became larger, and their amount was decreased considerably, *i.e.*, the coars-

Table 1
Young's modulus and hardness measured by nanoindentation

Phase	Al_2O_3 matrix	Al_2O_3 fiber	Ba–β-Al_2O_3
Young's modulus (GPa)	380 ± 9	355 ± 6	250 ± 15
Hardness (GPa)	25 ± 1	23 ± 2	20 ± 2

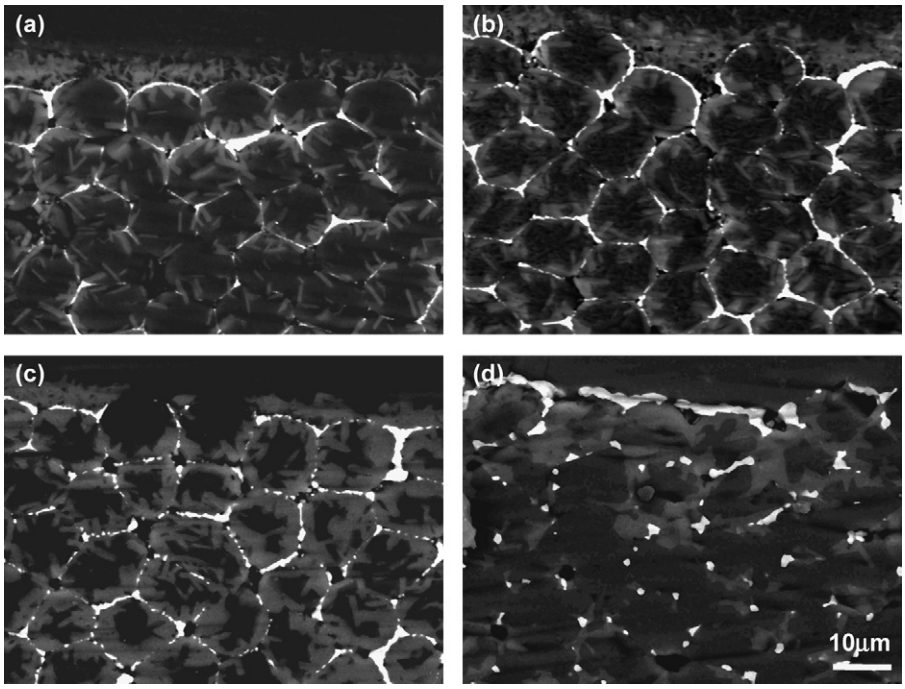

Fig. 5. Microstructures on polished cross-sections of the composites hot-pressed at 1300 °C, followed by heat treatment at (a) 1200 °C, (b) 1400 °C, (c) 1500 °C, and (d) 1600 °C.

ening of ZrO_2 particles occurred. It should be pointed out that some larger ZrO_2 particles might have dropped out during the preparation of samples for microstructural observations. On the other hand, the amount of the Ba–β-Al_2O_3 phase was reduced, relative to the microstructure at 1500 °C (Fig. 5(c)). The distribution of the Ba–β-Al_2O_3 phase seemed more inhomogeneous, for instance, almost no Ba–β-Al_2O_3 phase was present within some fibers and around the interfaces between the fibers. At the same time, however, some elongated Ba–β-Al_2O_3 phase was combined with each other, leading to the formation of larger light gray areas (Ba–β-Al_2O_3 compound).

Figs. 6 and 7 show the EPMA results of the specimens heat-treated at 1400 °C and 1600 °C, respectively. The morphology of ZrO_2 phase was quite different, but Zr was distributed at the interfaces between Al_2O_3 fibers in both cases. The distribution of Zr in Zr-rich areas (ZrO_2) was still inhomogeneous even at 1600 °C, although high-temperature treatment induced the breakup and spheroidization and/or coarsening of ZrO_2 particles. Similar to the microstructure without heat treatment (Fig. 2), there were higher Zr concentrations in the central regions of some large particles (Figs. 6(a) and 7(a)). With regard to Ba distribution map, the distribution range of Ba at 1400 °C was wider (Fig. 6(b)), and Ba concentration difference in Ba-rich areas seemed smaller, compared to as-hot-pressed specimen shown in Fig. 2(b). On the contrary, at 1600 °C, the distribution of Ba became more inhomogeneous. Within some fibers, almost no Ba–β-Al_2O_3 was present (marked by an arrow in Fig. 7(d)), while some large Ba–β-Al_2O_3 regions were formed simultaneously. These are consistent with the microstructural observations shown in Fig. 5.

Fig. 8 illustrates the damage in Young's modulus as a function of heat-treatment temperature. The damage parameter was very small and almost no change could be found up to 1400 °C. When the temperature was above 1400 °C, however, the damage in Young's modulus abruptly increased, *i.e.*, the Young's modulus value rapidly decreased. This change in Young's modulus value is believed to be related to the microstructural evolution, and it will be discussed in next section.

4. Discussion

4.1. Interfacial reaction behavior

From the results of microstructural observations, phase identifications, and compositional analyses described above, it is evident that the reactions between $BaZrO_3$ coating and Al_2O_3 fiber/matrix do occur under the hot-pressing conditions used in the current work. The chemical reactions between $BaZrO_3$ and Al_2O_3 can be written in the following general formula:

$$BaZrO_3 + xAl_2O_3 \rightarrow BaO{\cdot}xAl_2O_3 + ZrO_2 \quad (2)$$

Our previous investigation[37] has shown that the above reactions occur at ≥1200 °C, and x value mainly depends on the temperature under the conditions of excessive Al_2O_3. When $BaZrO_3$-coated Al_2O_3 fibers are heat-treated at lower temperatures (for example, <1300 °C), $x=1$, that is, barium monoaluminate ($BaAl_2O_4$ or $BaO{\cdot}Al_2O_3$) is formed. In $BaZrO_3$-coated Al_2O_3 fiber/Al_2O_3 matrix composites hot-pressed at 1300 °C, however, barium aluminate is present in the form of $BaO{\cdot}7.3Al_2O_3$ (*i.e.*, $x=7.3$ in Eq. (2)) or $BaAl_{14.66}O_{23}$ or $Ba_{0.75}Al_{11}O_{17.25}$), one of the nonstoichiometric hexaluminates or so-called Ba–β-Al_2O_3.

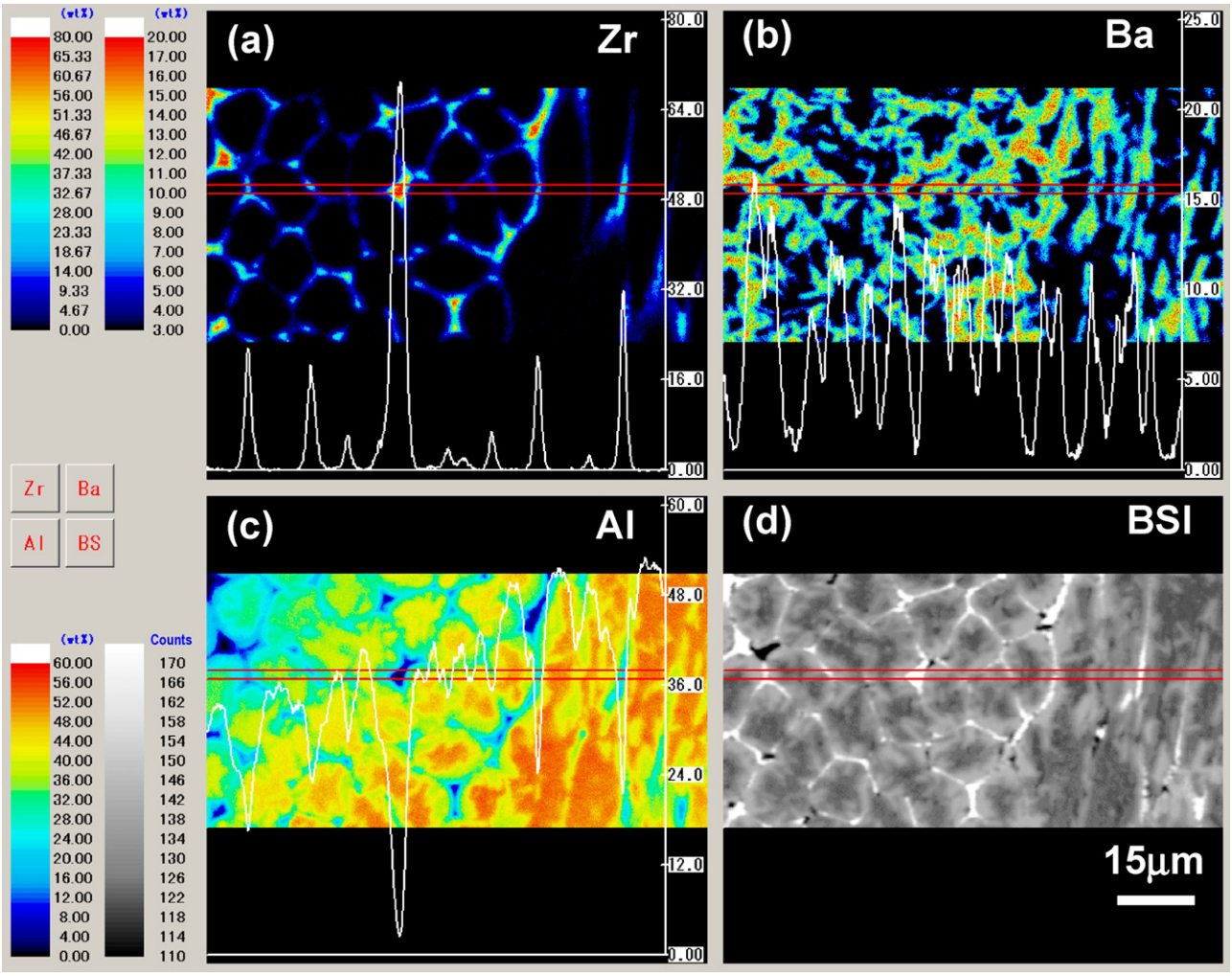

Fig. 6. Elemental distribution maps of (a) Zr, (b) Ba, and (c) Al as well as (d) corresponding backscattered electron image of heat-treated composites at 1400 °C.

Note that the Ba–β-Al_2O_3 compound has a composition close to $BaAl_{14.66}O_{23}$ from the XRD analysis in our previous work.[37,38] It should be pointed out that Ba–β-Al_2O_3 includes a number of nonstoichiometric compounds with a wide Al/Ba ratio in the range of 9.1–14.6.[44] It has been well established that stoichiometric barium hexaluminate ($BaAl_{12}O_{19}$ or $BaO{\cdot}6Al_2O_3$) is actually constituted by two nonstoichiometric phases, referred to as phase I and phase II, with compositions $BaAl_{14.66}O_{23}$ and $BaAl_{9.15}O_{14.73}$, respectively.[45,46] On the other hand, according to the phase diagram of Al_2O_3–$BaAl_2O_4$ system,[45] only phase I exists together with Al_2O_3, provided the molar fraction of BaO is less than 10%. In this work, the incorporation of a small amount of $BaZrO_3$ coating onto Al_2O_3 fibers (Al-rich) results in formation of monophasic $BaO{\cdot}7.3Al_2O_3$ in Al_2O_3 matrix. This is in good agreement with the result reported by Kimura et al.[45] Nevertheless, since the formation of Ba–β-Al_2O_3 phase is a solid-state diffusion process, there exists a concentration gradient of Ba during diffusion. Actually, we have confirmed the difference in Ba content in Ba-rich phase for as-hot-pressed specimen, as identified by EPMA (Fig. 2(b)). Accordingly, the x value in $BaO{\cdot}xAl_2O_3$ does not remain unchanged, and there may exist small amounts of barium aluminates with different Ba contents.

It is believed that the interfacial reactions between $BaZrO_3$ coating and Al_2O_3 fiber/matrix depend on the diffusion of Ba, Zr, and Al cations. Although the radius of Ba cation (0.13 nm) is larger than that of Zr (0.087 nm) or Al (0.057 nm) cation, as already mentioned, Ba has much larger diffusion distance than Zr or Al. This is possibly due to a smaller bond energy of BaO (573 kJ mol^{-1} at −273 °C [47]), compared to that of ZrO_2 (1448 kJ mol^{-1}) or Al_2O_3 (2209 kJ mol^{-1}). Hence, the diffusion of Ba cations dominates the reaction process between $BaZrO_3$ coating and Al_2O_3 fiber/matrix during hot pressing.

In hot-pressed composites, the majority of Ba cations in the initial $BaZrO_3$ coating have left the coating layers, giving rise to the formation of ZrO_2 (Zr-rich areas) at those sites where $BaZrO_3$ coating is originally present (*i.e.*, on the surfaces of fibers or interfaces between fibers). It seems that the resultant ZrO_2 phase contains small amounts of Ba and Al. The presence of Ba may be associated with the initial $BaZrO_3$ coating in which small amount of Ba remains, whereas the appearance of Al may be the result of diffusion or migration of Al from Al_2O_3 fiber/matrix towards the initial coating layers.

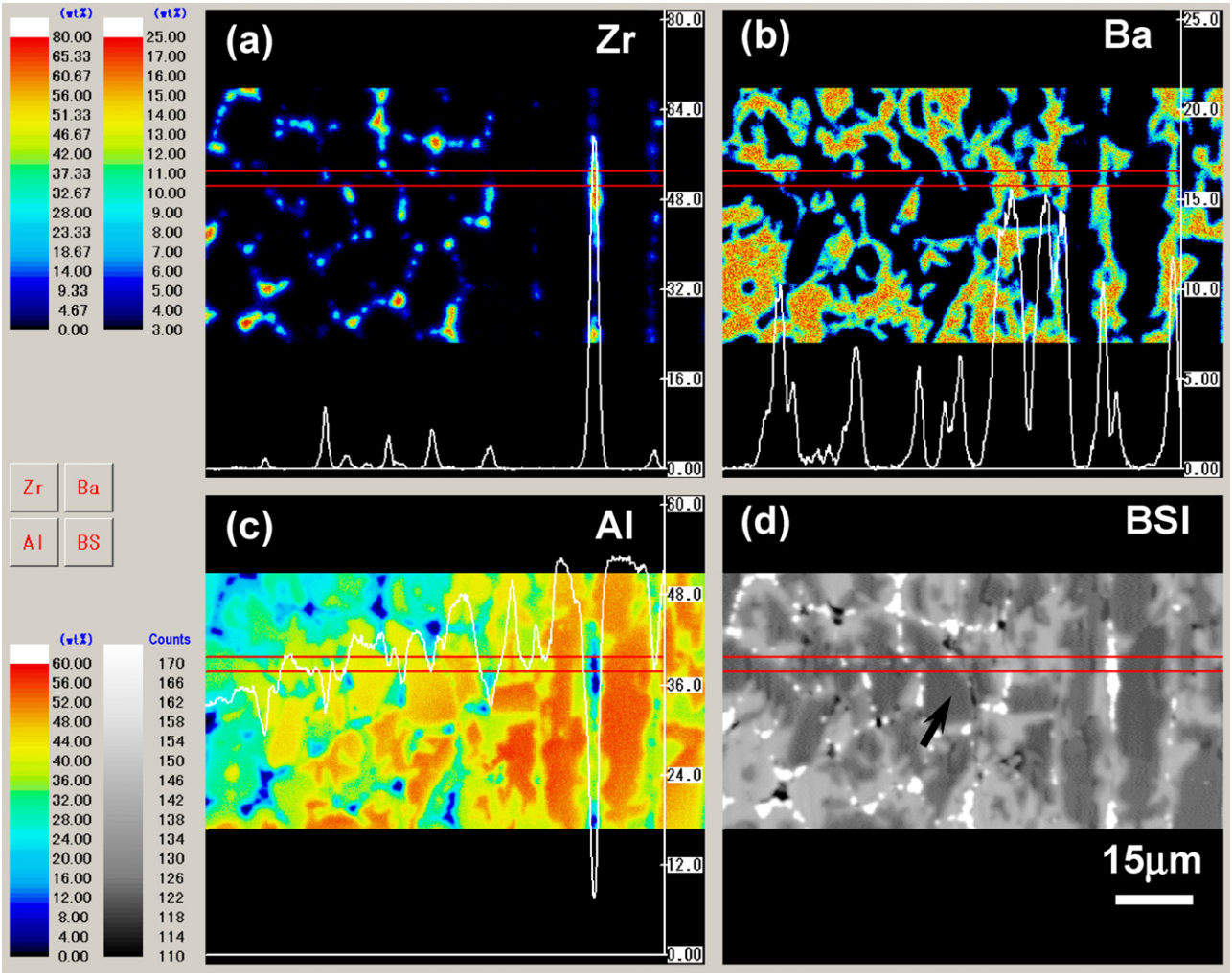

Fig. 7. Elemental distribution maps of (a) Zr, (b) Ba, and (c) Al as well as (d) corresponding backscattered electron image of heat-treated composites at 1600 °C.

It should be pointed out that there is electron beam broadening in EDS and EPMA analyses, which affects the accuracy of compositional analysis. In particular, for Zr-rich areas in the current work, they have similar dimensions to the interaction range between electron beam and sample. Thus, it is difficult to conclude the presence of Ba and Al in Zr-rich areas. In the case of Ba, however, the microstructural observations and compositional analyses reveal the occurrence of long-range diffusion of Ba cations. As a result of migration of Ba cations from $BaZrO_3$ coating to the surrounding Al_2O_3 fiber/matrix, Ba–β-Al_2O_3 phase is formed. Furthermore, this phase shows an elongated morphology. This microstructural feature is consistent with the Ba–β-Al_2O_3 reinforcements formed through reactive sintering of Al_2O_3 and $BaZrO_3$ powder mixtures,[48] and has also been found in other alkaline-earth and rare-earth hexaluminates such as $CaAl_{12}O_{19}$ [29] and $LaAl_{11}O_{18}$.[49] The elongated morphology of the Ba–β-Al_2O_3 phase may be attributed to its anisotropic growth habit. Since Ba–β-Al_2O_3 compound has a hexagonal structure with significantly different lattice parameters ($a = 0.5582$ nm and $c = 2.2715$ nm [50]), there may exist an interfacial or surface energy difference between the basal plane and other planes, which results in growth-rate anisotropy in different crystal planes and directions. Generally, hexaluminates grow with their basal planes parallel to the reaction direction because of rapid transport paths along the basal planes.[34] In this work, the orientational distribution of Ba and elongated

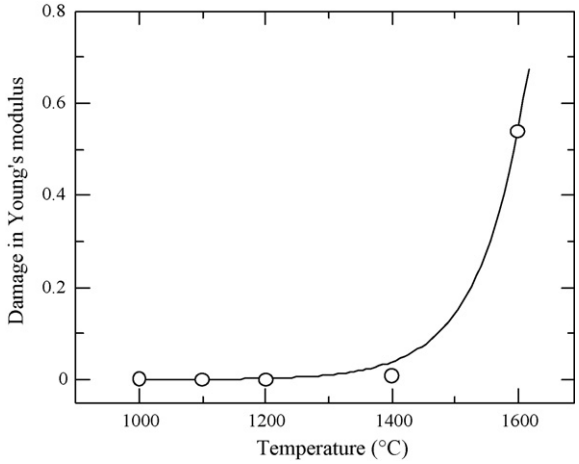

Fig. 8. Variation of damage in Young's modulus as a function of heat-treatment temperature.

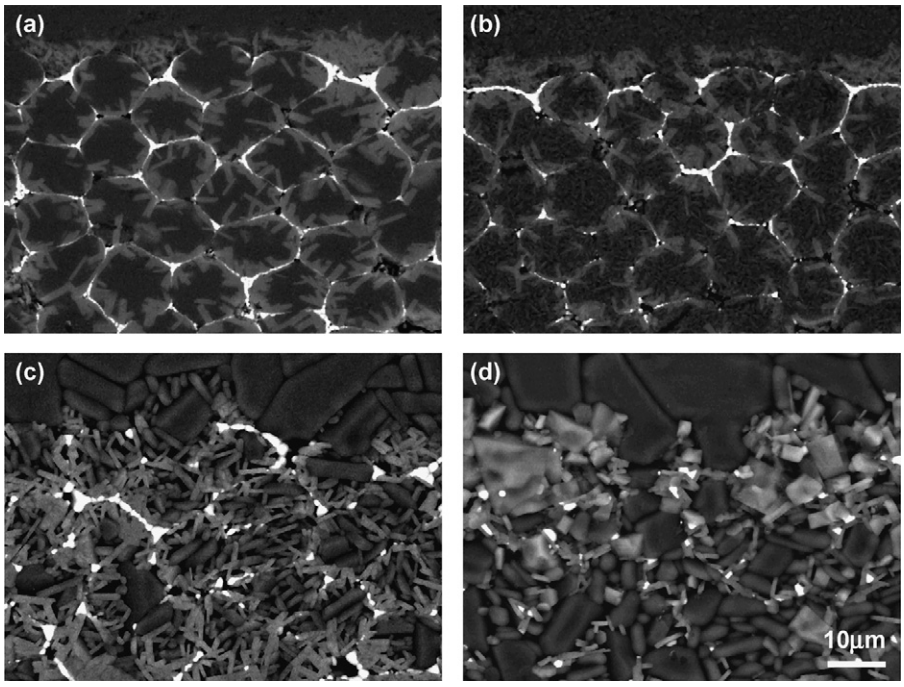

Fig. 9. Microstructures on surface layers (without polishing treatment after heat treatment) of heat-treated composites at (a) 1200 °C, (b) 1400 °C, (c) 1500 °C, and (d) 1600 °C.

morphology of Ba–β-Al_2O_3 particles are likely to result from preferential diffusion and mass transport of Ba along the basal plane.

It is known that Ba–β-Al_2O_3 compound has a layered crystal structure.[27,51] The appearance of the Ba–β-Al_2O_3 phase with an elongated morphology and layered structure is expected to cause improvements in fracture toughness. In fact, our previous work [48] showed that the formation of Ba–β-Al_2O_3 platelets in Al_2O_3 matrix leads to enhanced fracture toughness.

As can be seen in Fig. 1, the Ba–β-Al_2O_3 platelets formed *in situ* intruded into the surface areas of Al_2O_3 fibers. In particular, at those sites with more coating materials, because a lot of platelets coalesced into large reaction zones, the effective cross-sectional areas of fibers are reduced, possibly leading to the strength degradation of fibers. Consequently, to achieve an optimal combination of strength and fracture toughness, it is necessary to control the *in situ* interfacial reactions between the $BaZrO_3$ coating and Al_2O_3 fiber/matrix. This could be realized by adjusting the parameters of coating and densification processes, such as sol concentration, coating time, sintering temperature, and holding time. Further investigations on influence of processing conditions are necessary to optimize the mechanical properties of the composites.

4.2. Thermal stability

As mentioned previously, because of the reactions between $BaZrO_3$ coating and Al_2O_3 fiber/matrix, two reaction products, ZrO_2 and Ba–β-Al_2O_3, are formed in hot-pressed composites. Of these, ZrO_2 phase is continuously distributed at fiber/fiber and fiber/matrix interfaces. For simplicity, the morphology of ZrO_2 can be regarded as a cylindrical rod, which is unstable thermodynamically due to a large surface energy. The morphological instability of a long cylinder has been investigated by many researchers.[52–56] According to Rayleigh's perturbation theory,[52] a continuous cylinder is prone to development and growth of periodic axial oscillations in its radius. If the wavelength of perturbation (λ_{min}) is greater than the circumference $2\pi R$ (R is radius of the cylinder), the cylinder will eventually break up into a string of small discrete particles with a characteristic size and spacing, which are sensitive to the mass transport mechanism dominating the morphological evolution. As a consequence, during the heat treatment at elevated temperatures, continuous ZrO_2 at interfaces will break up into strings of spherical or equiaxed particles to reduce surface energy. The breakup and spheroidization may be realized through surface (interfacial) diffusion and/or lattice diffusion. From the microstructural observations and EPMA results described before, after heat treatment at elevated temperatures, although there exist morphological changes, ZrO_2 phase is still distributed at fiber/fiber and fiber/matrix interfaces. Furthermore, the diffusion distance of Zr to surrounding Al_2O_3 fiber/matrix is extremely small even when heat-treated at 1600 °C for 24 h (Fig. 7). Accordingly, the lattice diffusivity of Zr may be quite small. The breakup and spheroidization processes of ZrO_2 during heat treatment are considered to depend on the interfacial diffusion to a large extent.

With regard to the influence of heat treatment on stability of Ba–β-Al_2O_3 phase, as shown in Fig. 5(c), many new elongated Ba–β-Al_2O_3 particles have formed during the heat treatment at 1500 °C. One of the reasons for formation of new Ba–β-Al_2O_3 particles is believed to arise from the diffusion of Ba, which remains in Zr-rich areas after hot pressing, and then reacts with surrounding Al_2O_3 fibers. This mechanism, however, is

not satisfactory because it is difficult to explain why numerous Ba–β-Al_2O_3 particles are formed at 1500 °C, whereas many Ba–β-Al_2O_3 particles disappear again at a higher temperature (1600 °C).

To understand the evolution of Ba–β-Al_2O_3 phase during heat treatment, the microstructures on the surface layers of heat-treated specimens (without polishing treatment after thermal exposure) were examined. As shown in Fig. 9, the microstructures on specimen surfaces were similar to those inside specimens (Fig. 5) up to 1400 °C. After heat treatment at ≥1500 °C, the surfaces appeared uneven, and significant grain growth in Al_2O_3 phase occurred. At 1500 °C, numerous elongated Ba–β-Al_2O_3 particles were observed in the vicinity of the surface. This may be the result of migration of Ba cations from the interior to the exterior of the specimen, where they react with Al_2O_3. At higher temperatures (*e.g.*, 1600 °C), however, some Ba–β-Al_2O_3 particles seemed to disappear and some residual particles were combined into larger regions. This is considered to be due to the evaporation of BaO in Ba–β-Al_2O_3 phase, because BaO has a high partial pressure at elevated temperatures.[57] These results suggest that long-range migration of Ba, including both diffusion and evaporation, occurs during thermal exposure at 1600 °C.

Concerning the damage in Young's modulus, almost no change in Young's modulus was observed (Fig. 8) for composites heat-treated at ≤1400 °C, owing to their stable microstructures. As stated above, significant microstructural changes, including spheroidization and coarsening of ZrO_2 particles, migration of Ba cations and hence formation of new Ba–β-Al_2O_3 particles, and evaporation of BaO, occur during heat treatment at >1400 °C. Since Ba–β-Al_2O_3 phase exhibits a lower Young's modulus value than Al_2O_3 (Section 3.2), the formation of Ba–β-Al_2O_3 causes decrease in Young's modulus, while the evaporation of BaO leads to increase in Young's modulus. On the other hand, such processes as morphological evolution of ZrO_2, migration of Ba cations, and evaporation of BaO cause increase in porosity, which is considered to be one of the reasons for rapid decrease in Young's modulus (*i.e.*, increase in damage parameter). In fact, density measurements showed that the specimen hot-treated at 1600 °C had a density value of ∼5% lower than that of as-hot-pressed one. The dependence of Young's modulus on porosity can be expressed as [58]

$$E = E_0(1 - 1.9P + 0.9P^2) \quad (3)$$

where E is the modulus of the composite with pores, E_0 is the modulus of the composite with zero porosity, and P is the porosity in the composite. By substituting the data in Fig. 8 into Eq. (3), one can estimate that the porosity of heat-treated specimen at 1600 °C is as high as ∼34%, which is obviously a large overestimate over the microstructural observations. This reveals that the change in Young's modulus after heat treatment may be also related to some other factors in addition to the microstructural evolution described before. One possible reason is debonding at phase interfaces, which has been confirmed in sintered composites of partially stabilized zirconia and stainless steel.[59] In the current work, there may exist debonding at interfaces between Al_2O_3, ZrO_2, and Ba–β-Al_2O_3 phases, due to morphological change and existence of residual thermal stresses resulting from different coefficients of thermal expansion.

From the microstructural evolution and change in Young's modulus, it can be concluded that $BaZrO_3$-coated Al_2O_3 fiber/Al_2O_3 matrix composites have good thermal stability until 1400 °C. Above 1400 °C, the composite shows microstructural instability and hence degradation in mechanical properties.

5. Conclusions

A $BaZrO_3$ interphase was incorporated into Al_2O_3 fiber reinforced Al_2O_3 matrix composites through coating fibers via a sol–gel technique. The interfacial reaction behavior between $BaZrO_3$ coating and Al_2O_3 fiber/matrix during consolidation as well as thermal stability of the composites during thermal exposure at elevated temperatures have been investigated. The $BaZrO_3$ coating reacted *in situ* with Al_2O_3 fiber and surrounding Al_2O_3 matrix to form monoclinic ZrO_2 and Ba–β-Al_2O_3, one of the nonstoichiometric hexaluminate compounds during hot pressing. The resultant ZrO_2 was present at the initial coating layers on fiber surfaces, while Ba–β-Al_2O_3, exhibiting an elongated morphology (platelet), was distributed around fiber/fiber and fiber/matrix interfaces. The diffusion of Ba cations dominates the reaction process between $BaZrO_3$ coating and Al_2O_3 fiber/matrix during hot pressing. In comparison with Zr and Al, Ba exhibited much larger diffusion distance and preferred directional distribution. The formation of elongated Ba–β-Al_2O_3 phase may be attributed to preferred orientational growth through directional diffusion and mass transport of Ba along the basal plane. The micromechanical properties of the reaction products in the composites were evaluated by nanoindentation technique. The results showed that the Young's modulus and hardness of the Ba–β-Al_2O_3 phase are 250 GPa and 20 GPa, respectively.

$BaZrO_3$-coated Al_2O_3 fiber/Al_2O_3 matrix composites have good thermal stability during thermal exposure until 1400 °C. However, significant microstructural changes, including breakup, spheroidization and coarsening of ZrO_2 phase, migration of Ba cations and formation of new Ba–β-Al_2O_3 particles on surfaces, and evaporation of BaO, occur above 1400 °C. Continuous ZrO_2, distributed at fiber/fiber and fiber/matrix interfaces, can be broken up into strings of equiaxed particles through interfacial diffusion.

References

1. Chawla, K. K., *Ceramic Matrix Composites* (*2nd ed.*). Kluwer Academic Publishers, Boston, 2003.
2. Beesley, C. P., The application of CMCs in high integrity gas turbine engines. *Key Eng. Mater.*, 1997, **127–131**, 165–174.
3. Ohnabe, H., Masaki, S., Onozuka, M., Miyahare, K. and Sasa, T., Potential application of ceramic matrix composites to aero-engine composites. *Composites A*, 1999, **30**, 489–496.
4. More, K. L., Tortorelli, P. F., Ferber, M. K., Walker, L. R., Keiser, J. R., Miriyala, N. *et al.*, Exposure of ceramics and ceramic matrix composites in simulated and actual combustor environments. *Trans. ASME J. Eng. Gas Turbines Power*, 2000, **122**, 212–218.

5. DiCarlo, J. A. and Yun, H. M., Modeling the thermostructural capability of continuous fiber-reinforced ceramic composites. *Trans. ASME J. Eng. Gas Turbines Power*, 2002, **124**, 465–470.
6. McMahon, T. J., Advanced hot gas filter development. *Ceram. Eng. Sci. Proc.*, 2000, **21**, 47–57.
7. Davis, J. B., Marshall, D. B., Oka, K. S., Housley, R. M. and Morgan, P. E. D., Ceramic composites for thermal protection systems. *Composites A*, 1999, **30**, 483–488.
8. Klemm, H., Corrosion of silicon nitride materials in gas turbine environment. *J. Eur. Ceram. Soc.*, 2002, **22**, 2735–2740.
9. Evans, A. G. and Zok, F. W., The physics and mechanics of fiber-reinforced brittle-matrix composites. *J. Mater. Sci.*, 1994, **29**, 3857–3896.
10. Chawla, K. K., Xu, Z. R., Venkatesh, R. and Ha, J. S., Interface engineering in some oxide/oxide composites. In *Proceedings of the ninth International Conference on Composite Materials*, 1994, pp. 788–795.
11. Chawla, K. K., Ferber, M. K., Xu, Z. R. and Venkatesh, R., Interface engineering in alumina/glass composites. *Mater. Sci. Eng. A*, 1993, **162**, 35–44.
12. Lundberg, R., Pejryd, L., Butler, E., Ekelund, M. and Nygren, M., Development of oxide composites. In *Proceedings of the International Conference on High Temperature Ceramic Matrix Composites I*, ed. R. Naslain, J. Lamon and D. Doumeingts. Woodhead Publication, UK, 1993, pp. 167–174.
13. Davis, J. B., Loefvander, J. P. A., Evans, A. G., Bischoff, E. and Emiliani, M. L., Fiber coating concepts for brittle-matrix composites. *J. Am. Ceram. Soc.*, 1993, **76**, 1249–1257.
14. Lewis, M. H., Cain, M. G., Doleman, P., Razzell, A. G. and Gent, J., Development of interfaces in oxide and silicate matrix composites. In *High-Temperature Ceramic-Matrix Composites II*, ed. A. G. Evans and R. Naslain. American Ceramic Society, Westerville, OH, 1995, pp. 41–52.
15. Lev, L. C. and Argon, A. S., Oxide-fiber-oxide-matrix composites. *Mater. Sci. Eng. A*, 1995, **195**, 251–261.
16. Dong, R. and Hirata, Y., Processing of ceria-coated alumina fiber/alumina matrix composite. *J. Ceram. Soc. Jpn.*, 2000, **108**, 823–829.
17. Lewis, M. H., Tye, A., Butler, E. G. and Doleman, P. A., Oxide CMCs: interphase synthesis and novel fibre development. *J. Eur. Ceram. Soc.*, 2000, **20**, 639–644.
18. Morgan, P. E. D. and Marshall, D. B., Ceramic composites of monazite and alumina. *J. Am. Ceram. Soc.*, 1995, **78**, 1553–1563.
19. Cain, M. G., Cain, R. L., Tye, A., Rian, P., Lewis, M. H. and Gent, J., Structure and stability of synthetic interphases in CMCs. *Key Eng. Mater.*, 1997, **127–131**, 37–50.
20. Kuo, D.-H., Kriven, W. M. and Mackin, T. J., Control of interfacial properties through fiber coatings: monazite coatings in oxide-oxide composites. *J. Am. Ceram. Soc.*, 1997, **80**, 2987–2996.
21. Davis, J. B., Marshall, D. B. and Morgan, P. E. D., Oxide composites of Al_2O_3 and $LaPO_4$. *J. Eur. Ceram. Soc.*, 1999, **19**, 2421–2426.
22. Chawla, K. K., Liu, H., Janczak-Rausch, J. and Sambasivan, S., Microstructure and properties of monazite ($LaPO_4$)-coated saphikon fiber/alumina matrix composites. *J. Eur. Ceram. Soc.*, 2000, **20**, 551–559.
23. Morgan, P. E. D. and Marshall, D. B., Functional interfaces for oxide/oxide composites. *Mater. Sci. Eng. A*, 1993, **162**, 15–25.
24. Cinibulk, M. K., Magnetoplumbite composites as a fiber coating in oxide/oxide composites. *Ceram. Eng. Sci. Proc.*, 1994, **15**, 721–728.
25. Cinibulk, M. K., Hexaluminates as a cleavable fiber-matrix interphase: synthesis, texture development, and phase compatibility. *J. Eur. Ceram. Soc.*, 2000, **20**, 569–582.
26. Hitchcock, D. C. and DeJonghe, L. C., Fracture-toughness anisotropy of sodium beta-alumina. *J. Am. Ceram. Soc.*, 1983, **66**, C-204–C-205.
27. Iyi, N., Takekawa, S. and Kimura, S., Crystal chemistry of hexaaluminates: β-alumina and magnetoplumbite structures. *J. Solid State Chem.*, 1989, **83**, 8–19.
28. Morgan, P. E. D. and Miles, J. A., Magnetoplumbite-type compounds: further discussion. *J. Am. Ceram. Soc.*, 1986, **69**, C157–C159.
29. Cinibulk, M. K. and Hay, R. S., Textured magnetoplumbite fiber-matrix interphase derived from sol–gel fiber coatings. *J. Am. Ceram. Soc.*, 1996, **79**, 1233–1246.
30. Parthasarathy, T. A., Boakye, E., Cinibulk, M. K. and Petry, M. D., Fabrication and testing of oxide/oxide microcomposites with monazite and hibonite as interlayers. *J. Am. Ceram. Soc.*, 1999, **82**, 3575–3583.
31. Cinibulk, M. K., Effect of divalent cations on the synthesis of citrate-gel-derived lanthanum hexaluminate powders and films. *J. Mater. Res.*, 1999, **14**, 3581–3593.
32. Cinibulk, M. K., Deposition of oxide coatings on fiber cloths by electrostatic attraction. *J. Am. Ceram. Soc.*, 1997, **80**, 453–460.
33. Cinibulk, M. K., Effect of precursors and dopants on the synthesis of sol–gel-derived calcium hexaluminate. *J. Am. Ceram. Soc.*, 1998, **81**, 3157–3168.
34. Cain, M. G., Cain, R. L. and Lewis, M. H., *In situ* reacted rare-earth hexaaluminate interphases. *J. Am. Ceram. Soc.*, 1997, **80**, 1873–1876.
35. Gladysz, G. M., Schmuecker, M., Chawla, K. K., Schneider, H., Joslin, D. L. and Ferber, M. K., Characterization of the reaction products that develop in the processing of $Al_2O_3/BaZrO_3$ laminated compounds. *Mater. Character.*, 1998, **40**, 209–214.
36. Koopman, M., Duncan, S., Chawla, K. K. and Coffin, C., Processing and characterization of barium zirconate-coated alumina fiber/alumina matrix composites. *Composites A*, 2001, **32**, 1039–1044.
37. Chen, Z. C., Duncan, S., Chawla, K. K., Koopman, M. and Janowski, G. M., Characterization of interfacial reaction products in alumina fiber/barium zirconate coating/alumina matrix composite. *Mater. Character.*, 2002, **48**, 305–314.
38. Chen, Z. C., Kulkarni, R., Chawla, K. K., Koopman, M. and Ikeda, K., Processing and microstructure of an all-oxide ceramic composite. *Mater. Sci. Forum*, 2005, **475–479**, 1301–1304.
39. Li, X. and Bhushan, B., A review of nanoindentation continuous stiffness measurement technique and its application. *Mater. Character.*, 2002, **48**, 11–36.
40. Lemaitre, J., *A Course on Damage Mechanics*. Springer-Verlag, Berlin, 1992.
41. Galusek, D., Twigg, P. C. and Riley, F. L., Wet erosion of liquid phase sintered alumina. *Wear*, 1999, **233–235**, 588–595.
42. Twigg, P. C., Riley, F. L. and Roberts, S. G., Nanoindentation investigation of micro-fracture wear mechanisms in polycrystalline alumina. *J. Mater. Sci.*, 2002, **37**, 845–853.
43. Stollberg, D. W., Hampikian, J. M., Riester, L. and Carter, W. B., Nanoindentation measurements of combustion CVD Al_2O_3 and YSZ films. *Mater. Sci. Eng. A*, 2003, **359**, 112–118.
44. Groppi, G., Cristiani, C. and Forzatti, P., Phase composition and mechanism of formation of Ba–β-alumina-type systems of catalytic combustion prepared by precipitation. *J. Mater. Sci.*, 1994, **29**, 3441–3450.
45. Kimura, S., Bannai, E. and Shindo, I., Phase relations relevant to hexagonal barium aluminates. *Mater. Res. Bull.*, 1982, **17**, 209–215.
46. Iyi, N., Takekawa, S., Bando, Y. and Kimura, S., Electron-microscopic study of barium hexaluminates. *J. Solid State Chem.*, 1983, **47**, 34–40.
47. Vedeneyev, V. I., Gurvich, L. V., Kondrat'yev, V. N., Medvedev, V. A. and Frankeich, Ye. L., *Bond Energies, Ionization Potentials and Electron Affinities, Translated from the Russian by Scripta Technica Ltd.*. St Martin's Press, New York, 1966.
48. Chen, Z. C., Chawla, K. K. and Koopman, M., Microstructure and mechanical properties of *in situ* synthesized alumina/Ba–β-alumina/zirconia composites. *Mater. Sci. Eng. A*, 2004, **367**, 24–32.
49. Jang, B.-K. and Kishi, T., Fabrication and microstructure of Al_2O_3 matrix composites by *in situ* reaction in the Al_2O_3–La_2O_3 system. *J. Ceram. Soc. Jpn.*, 1998, **106**, 739–743.
50. van Berkel, F. P. F., Zandbergen, H. W., Verschoor, G. C. and Ijdo, D. J. W., The structure of barium aluminate $Ba_{0.75}Al_{11}O_{17.25}$. *Acta Cryst.*, 1984, **C40**, 1124–1127.
51. Park, J.-G. and Cormack, A. N., Crystal/defect structure and phase stability in Ba hexaluminates. *J. Solid State Chem.*, 1996, **121**, 278–290.
52. Rayleigh, L., On the instability of jets. *Proc. London Math. Soc.*, 1879, **10**, 4–13.
53. Nichols, F. A. and Mullins, W. W., Surface- (interface-) and volume-diffusion contributions to morphological changes driven by capillarity. *Trans. AIME*, 1965, **233**, 1840–1848.

54. Cline, H. E., Shape instability of eutectic composites at elevated temperatures. *Acta Metall.*, 1971, **19**, 481–490.
55. Stüwe, H. P. and Kolednik, O., Shape instability of thin cylinders. *Acta Metall.*, 1988, **36**, 1705–1708.
56. Ma, Q., Liu, B. and Li, R., Thermodynamic considerations of the equilibrium shape of an infinitely long rod. *Acta Metall.*, 1994, **42**, 4083–4086.
57. Odoj, R. and Hilpert, K., Evaporation and standard enthalpy of formation of $BaZrO_3$(s). *Z. Phys. Chem. Neue Folge*, 1976, **102**, 191–201.
58. Phillips, D. C., Sambell, R. A. J. and Bowen, D. H., Mechanical properties of carbon fiber reinforced pyrex glass. *J. Mater. Sci.*, 1972, **7**, 1454–1464.
59. Yamada, Y., Kawasaki, A., Taya, M. and Watanabe, R., Effect of debonding at the phase interface on Young's modulus in sintered PSZ/stainless steel composite. *J. Jpn. Inst. Met.*, 1994, **58**, 162–168.